

# Ultrafast Laser Induced Structural Modification of Fused Silica—Part II: Spatially Resolved and Decomposed Raman Spectral Analysis

Siniša Vukelić

Panjawat Kongsuwan

Department of Mechanical Engineering,  
Columbia University,  
New York, NY 10027

Sunmin Ryu

Department of Chemistry,  
Columbia University,  
New York, NY 10027

Y. Lawrence Yao

Department of Mechanical Engineering,  
Columbia University,  
New York, NY 10027

*Nonlinear absorption of femtosecond laser pulses enables the induction of structural changes in the interior of bulk transparent materials without affecting their surface. In the present study, femtosecond laser pulses were tightly focused within the interior of bulk fused silica specimen. Localized plasma was formed, initiating rearrangement of the random network structure. Cross sections of the induced features were examined via decomposition of spatially resolved Raman spectra and a new method for the quantitative characterization of the structure of amorphous fused silica was developed. The proposed method identifies the volume fraction distribution of ring structures within the continuous random network of the probed volume of the target material and changes of the distribution with laser process conditions. Effects of the different process conditions and the material response to different mechanisms of feature generation were discussed as well. [DOI: 10.1115/1.4002768]*

## 1 Introduction

In recent times, advances in femtosecond (fs) laser development have led to a wide spectrum of new applications [1]. One of the main advantages of femtosecond lasers in comparison to nanosecond lasers is that they induce much less collateral damage due to heat conduction [2]. Furthermore, nonlinear absorption, a unique property of femtosecond lasers, makes them particularly suitable for treatment of dielectric materials [3].

The potential of creating three-dimensional optical storage devices [4] has led to the study of the interaction of various transparent materials with ultrafast laser pulses. Glezer and Mazur [5] showed that femtosecond laser pulses tightly focused into the interior of the glass with an energy level near the damage threshold produce submicron cavities or voxels. These structures are characterized by a change in refractive index and consist of a centrally placed void or area of less dense material accompanied by a denser surrounding region. Bellouard et al. [6] studied fs-laser induced changes in the morphology of fused silica through its effects on etching selectivity, increase of internal stresses, and densification. Schaffer et al. [7–9] explored different aspects of ultrafast laser fused silica interaction. Topics covered included the potential of micromachining bulk glass with the use of nanojoule energy pulses, the bulk heating of transparent materials, and the morphology of structural changes induced by femtosecond lasers. Kucheyev and Demos [10] used photoluminescence (PL) and Raman spectroscopy to characterize defects created in the amorphous fused silica irradiated by nanosecond and femtosecond lasers with different wavelengths. Their PL results have shown that laser irradiation causes the forming of nonbridging oxygen hole centers (NBOHC) and oxygen-deficiency centers (ODC). Raman spectroscopy revealed the densification of the irradiated area. Chan et al. [11] used a femtosecond laser to irradiate the interior of a fused silica slab and performed in situ Raman spectroscopy

measurements. Atomic-scale structural changes were observed that led to the densification of the affected material. The induced damage was related to changes in other properties obtained for vitreous silica using different treatments.

The molecular structure of the fused silica was studied through employment of Raman scattering. Different vibrational bands have been associated with particular ring structures in a random network configuration. Altering its structure has been studied via utilization of neutron bombardment. It is reported that the densification of the fused silica glass has been observed in neutron irradiated samples. Bombardment with neutrons causes different responses from 440  $\text{cm}^{-1}$ , 495  $\text{cm}^{-1}$ , and 606  $\text{cm}^{-1}$  bands, which is associated with the conversion of five-, six-, and other higher membered rings into four-membered rings [12]. A fictive temperature increase has the effect of increasing the intensity of the 495  $\text{cm}^{-1}$  and 606  $\text{cm}^{-1}$  bands [13,14], suggesting that higher density structure is responsible for these modes. More recently, Chan et al. [11] used Raman scattering to investigate the effects of femtosecond laser irradiation on the interior of fused silica. They showed that ultrafast laser treatment causes a relative increase in the intensity of the 495  $\text{cm}^{-1}$  and 606  $\text{cm}^{-1}$  bands with respect to the main peak (440  $\text{cm}^{-1}$ ) and showed that this increase is a function of the incident laser energy. The area under the increased peak is qualitatively associated with the densification of the material.

The work reviewed above addresses changes in properties and morphology, which are consequences of structural alterations induced by ultrafast laser irradiation of the interior of transparent materials. It also somewhat explains the physical process that leads to those changes. In the study presented here, the focus is on the atomistic level and rearrangement of the ring structures of amorphous fused silica. Spatially resolved Raman spectroscopy is employed as a nondestructive characterization technique to show local densification and relative volume fraction changes of the ring structures within the focal volume and in the surrounding region. A more detailed analysis of Raman scattering of fused silica specimens treated by ultrafast lasers is performed. A new

Contributed by the Manufacturing Engineering Division of ASME for publication in the JOURNAL OF MANUFACTURING SCIENCE AND ENGINEERING. Manuscript received July 27, 2010; final manuscript received August 8, 2010; published online December 17, 2010. Editor: K. F. Ehmann.

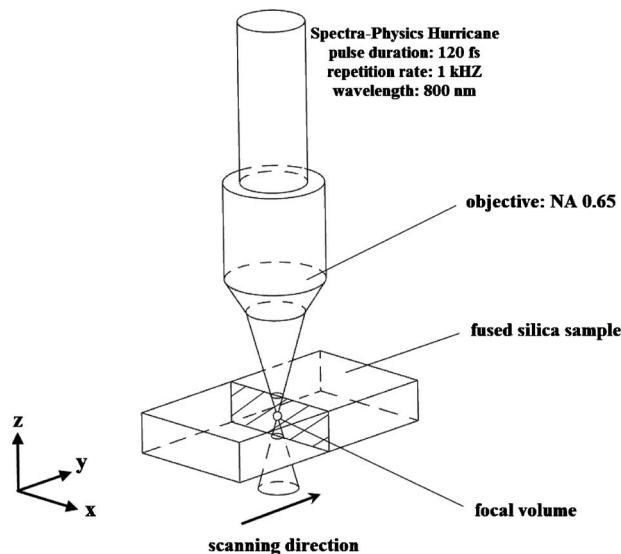


**Fig. 1** Schematic illustration experimental setup. The shaded plane (cross section) shows that the laser beam is focused to the interior of our fused silica sample. Laser beam scanning direction is along  $y$ -axis.

method based on spectral decomposition to quantitatively determine the percentage of different ring structures within the probed volume is proposed.

## 2 Experimental Setup and Characterization

An amplified Ti-sapphire laser system, Spectra-Physics Hurricane with pulse duration of 120 fs at 1 kHz repetition rate and 800 nm wavelength was used to conduct experiments. A Zeiss Plan Neofluar 40 $\times$  objective lens with numerical aperture (NA) of 0.65 was employed to focus the laser, providing approximately a 1.5  $\mu\text{m}$  spot size. The beam was focused within the interior of the 1.6 mm thick, 20 mm square S1-UV grade fused silica glass specimen mounted on an Aerotech motorized linear stage to create localized structural changes. A schematic diagram of the experiment setup can be seen in Fig. 1. A number of different conditions were applied by varying the feed rate of the stage and the energy of the laser pulses. Pulses were applied at energies ranging from 2  $\mu\text{J}$  to 35  $\mu\text{J}$  and stage velocities varied from 0.04 mm/s to 1 mm/s.

After the fs-laser treatment, the affected region was examined via micro-Raman spectroscopy to characterize structural changes. Raman spectra were obtained in a back scattering geometry using a 40 $\times$  objective with a correction collar, which compensates for optical aberrations caused by the intervening fused silica material. The excitation wavelength was 514.5 nm (Ar ion laser) and the laser power at the sample was 14 mW. To filter out scattering and luminescence from the material outside the focal volume, a 50  $\mu\text{m}$  pinhole was placed in front of the spectrometer. The spectral resolution was found to be 6  $\text{cm}^{-1}$ . Three representative conditions at the same energy level of 30  $\mu\text{J}$  and feed rates of 0.04 mm/s, 0.5 mm/s, and 1 mm/s are studied. Spatial mapping of the cross section was performed with 1  $\mu\text{m}$  spacing in the  $x$ -direction and 5  $\mu\text{m}$  spacing in the  $z$ -direction in the cases when 1 mm/s and 0.5 mm/s feed rates were used for feature generation and 2  $\mu\text{m}$  spacing in the  $x$ -direction and 10  $\mu\text{m}$  spacing in the  $z$ -direction was employed for characterization of the cross section of the line generated at 0.04 mm/s stage velocity. The difference in spatial resolution is due to the size of the feature on the cross section.

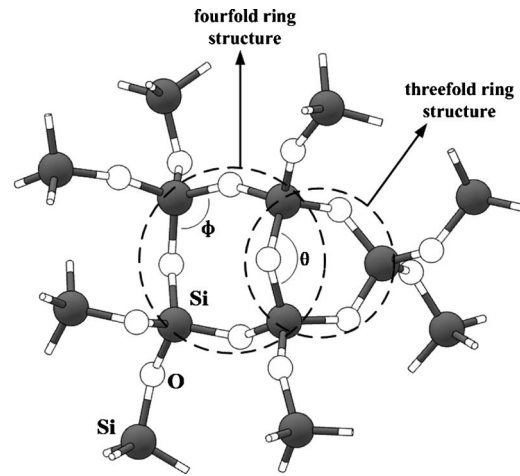


**Fig. 2** Ball and stick model of the random network in the fused silica, showing threefold and fourfold ring structures (encircled)

## 3 Formation of the Ring Structures in Fused Silica

One of the main characteristics of amorphous solids is the lack of regularly repeating groups of atoms, which are native to crystalline materials. Amorphous fused silica belongs to the group of so-called associated liquids [15], which form bonds in definite vectorial positions in space, leading to the formation of ring structures that connect molecules. Ring distribution can further be defined via shortest path analysis. In this method, an oxygen atom is connected to two silicon atoms in the path such that the smallest possible ring is formed [15,16]. In the case of amorphous solids, these rings then form a random network. A random network of atoms in fused silica is illustrated in Fig. 2. In fused silica, ring structures consist of tetrahedral atomic arrangements, suggesting that the basic structural unit of such amorphous materials is a tetrahedron.

Due to the lack of a theory to connect properties at the micro- and macroscales, the structure of glasses is analyzed through the creation of statistical models. Two types of models can be found in literature. In the first model, silicon and oxygen atoms are represented by spheres connected with wires [17]. This model is idealized in the sense that it does not take into account defects or impurities. The second model is based on atomic interactions. This model relies on statistical mechanics and interactions are governed by a molecular dynamics method as more recently reported [16,18].

Employing the molecular dynamic method, one can gain insight into the fused silica network through discussion of  $n$ -fold rings. The basic structural unit consists of silicon atom surrounded by four oxygen atoms. There are six different ways to form a closed path starting from a structure denoted as  $\text{O}_1\text{-Si}_1\text{-O}_2$ , and one looks for the shortest path to form a ring. Statistical analysis is used to calculate distribution of the  $n$ -fold rings.

Most of the ring structures contain five or six ring members. This is due to the fact that the angle between  $\text{O-Si-O}$  bonds is approximately 133 deg, suggesting that larger ring structures are formed from almost perfect tetrahedrons, which require minimal strain energy for their formation. In contrast, the formation of three and four member rings requires smaller  $\text{O-Si-O}$  angles (around 102 deg and 109 deg, respectively) [19], which has the consequence of distorting the tetrahedrons that create these ring structures. Thus, the strain energy required for the formation of these rings is higher than for the formation of  $n \geq 5$ -membered rings.

#### 4 Raman Spectroscopy in $AX_2$ Glasses

The class of  $AX_2$  glasses to which  $SiO_2$  belongs forms a three-dimensional continuous random network made of linked  $AX_4$  tetrahedrons. The structure and vibrational properties of  $AX_2$  glasses have been studied theoretically and experimentally. A theoretical approach through employment of a central force model was introduced by Sen and Thorpe [20]. The model studies vibrational densities of  $AX_2$  glasses, such as  $SiO_2$  and  $GeO_2$ , through investigation of the basic unit of the network, a five-atom tetrahedron. Bond distances between the atoms in the tetrahedrons are the same, and the bond angle in the  $A-X-A$  bridge, represented by  $\theta$ , is constant for the entire network. Assuming that noncentral forces are negligible and the central force  $\alpha$  (bond-stretching) is constant, San and Thorpe [20] used potential energy and the equations of motion of bonds to obtain angular frequencies

$$V = \frac{\alpha}{2} \sum_{\langle ij \rangle} [(u_i - u_j) \times r_{ij}]^2 \quad (1)$$

$$\begin{aligned} (M\omega^2 - \alpha)u_1 &= -\left(\alpha \sin \frac{\theta}{2}\right)x - \left(\alpha \cos \frac{\theta}{2}\right)y \\ \left(m\omega^2 - 2\alpha \sin^2 \frac{\theta}{2}\right)x &= -\left(\alpha \sin \frac{\theta}{2}\right)u_1 + \left(\alpha \sin \frac{\theta}{2}\right)u_2 \\ \left(m\omega^2 - 2\alpha \cos^2 \frac{\theta}{2}\right)y &= -\left(\alpha \cos \frac{\theta}{2}\right)u_1 - \left(\alpha \cos \frac{\theta}{2}\right)u_2 \end{aligned} \quad (2)$$

where  $u_i$  and  $u_j$  are displacements,  $r$  is the unit vector in the direction of the bond,  $m$  and  $M$  are the mass of atoms  $X$  and  $A$ , respectively, and  $\omega_i$  are angular frequencies. After derivation [20], angular frequencies are given as functions of intertetrahedral angle  $\theta$

$$\begin{aligned} \omega_1^2 &= (\alpha/m)(1 + \cos \theta) \\ \omega_2^2 &= (\alpha/m)(1 - \cos \theta) \\ \omega_3^2 &= \omega_1^2 + (4\alpha/3M) \\ \omega_4^2 &= \omega_2^2 + (4\alpha/3M) \end{aligned} \quad (3)$$

Angular frequencies obtained from Eq. (3) are responsible for the following atomic motions [21,22]:  $\omega_1$  represents pure bending motion of the  $X$  atom, which, in the case of amorphous,  $SiO_2$  is the motion of the bridging oxygen along the axis that bisects the  $Si-O-Si$  bond angle,  $\omega_2$  is associated with the rocking of the bridging atom,  $\omega_3$  is composed of pure bending (symmetric stretch) and some motion of the  $A$  atom, and lastly,  $\omega_4$  is the antisymmetric motion of the  $X$  atom parallel to the  $A-A$  line. As the intertetrahedral angle is distributed about some value, ( $SiO_2$ , 133 deg) these frequencies, which can be replaced without loss of accuracy with wave numbers [22], represent central positions of the bands in the Raman spectra. Typical polarized Raman spectra of an as-received fused silica sample is shown in Fig. 3, and theoretical values of angular frequencies [22] are superimposed on it. Our study is focused on the analysis of the main, dominant band with its central peak located at 440  $cm^{-1}$ . Furthermore, all but  $\omega_1$  frequencies are infrared active [22,23], which involves separation of the band into transverse-optical excitations and longitudinal-optical excitations, also known as TO-LO pair [23]. Presence of these pairs has a consequence in splitting of the Raman bands, which is very clearly seen for  $\omega_4$  frequency in Fig. 3, and makes analysis of these bands difficult.

As discussed in Sec. 3, the structure of  $AX_2$  glasses consists of  $n$ -fold rings and the number of atoms present in the ring directly influences the intertetrahedral angle  $\theta$ . Each of the  $n$ -fold ring structures present in the random network has a particular vibration frequency, or more precisely narrow band, due to the angle  $\theta$

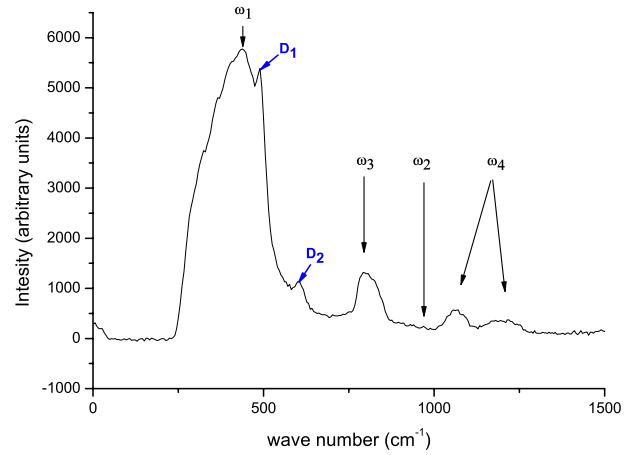


Fig. 3 Typical Raman spectra of as-received fused silica sample

between tetrahedral components of the ring. Therefore, the main band in the Raman spectra of fused silica, as shown in Fig. 3, denoted as  $\omega_1$  can be resolved into a peak located at 440  $cm^{-1}$ , which corresponds to the molecular vibration of the five- and sixfold ring structures [15] and two subpeaks located at 495  $cm^{-1}$  and 606  $cm^{-1}$  and denoted as  $D_1$  and  $D_2$  in Fig. 3, that correspond to the molecular vibration of the fourfold ( $\theta=109$  deg) and threefold ( $\theta=102$  deg) ring structures [19], respectively. Moreover, broadening of the band is associated with the presence of higher order rings [15].

#### 4.1 Curve Fitting of Raman Spectra

**4.1.1 Nature of the Line-Profile of Single Band in Raman Spectra.** In many applications and research studies, overlapping of individual Raman bands is quite common. Thus, sometimes, it is quite tricky to quantify the influence of particular bands on the entire spectra. One approach is to perform a curve fit employing a function that consists of a set of individual bands. The most important aspect of curve fitting is appreciating the underlying physics behind the vibrational spectra. The nature of single band line-profiles obtained from Raman spectra can be derived either by employing hydrodynamic theory or by relating molecular vibrations to the model of a harmonic oscillator subject to an oscillating external force and friction. The latter approach was described by Marshall and Verdun [24] and was briefly summarized below.

The line shape in vibrational spectra can be understood from the mass and spring model. Power absorption in the spectrum corresponds to the frequency of the spring and the damping coefficient can be related to the width of the spectral line of interest. If we adopt this analogy, the equation of motion can be written as

$$m \frac{d^2x}{dt^2} = -kx - f \frac{dx}{dt} + F_o \cos \omega t \quad (4)$$

where  $-kx$  represents the restoring force from the spring,  $-f(dx/dt)$  is the friction suppressing the motion,  $F_o \cos \omega t$  is the external sinusoidally oscillating driving force, and  $x$  is the steady state displacement that can be decomposed into two components  $x'$  and  $x''$ , which represent dispersion and absorption spectra, respectively. In other words, the analogy can be explained as the weight-on-a-spring being an electron bound to an atom or molecule and the driving force being the oscillation of the electric field of a light wave. From the equation of the motion, Eq. (4), one can obtain an expression for the absorption

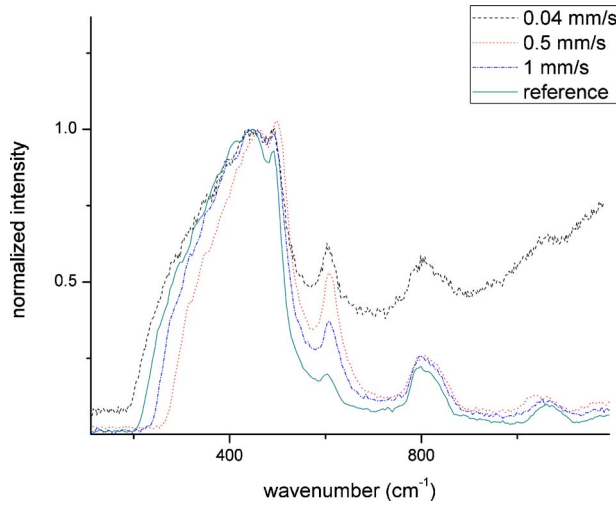


**Fig. 4 Typical normalized Raman spectra reference and spectra from fused silica processed with pulse energy: 30  $\mu\text{J}$  at feed rates 0.04 mm/s, 0.5 mm/s, and 1 mm/s**

$$x'' = F_o \left( \frac{f\omega}{m^2(\omega_o^2 - \omega^2) + f^2\omega^2} \right) \quad (5)$$

where  $\omega_o = \sqrt{k/m}$ . From Eq. (5), it can be seen that a single band in an absorption spectra is actually of a Lorentzian profile type.

**4.1.2 Curve Fitting.** The Levenberg–Marquardt algorithm has been employed for the curve fitting of the Raman spectra. It represents a maximum neighborhood method developed through interpolation between the Taylor series method and the gradient descent method. Similar to most least-squares estimation algorithms, it sets a problem as the iterative solving of a set of nonlinear algebraic equations

$$E(y) = f(x_1, x_2, \dots, x_m, \beta_1, \beta_2, \dots, \beta_k) = f(x, \beta) \quad (6)$$

where  $x_1, x_2, \dots, x_m$  are the independent variables,  $\beta_1, \beta_2, \dots, \beta_k$  are the population values of  $k$  parameters, and  $E(y)$  is the expected value of the independent variable. The solution represents a set of parameters obtained such that minimization of the following equation takes place:

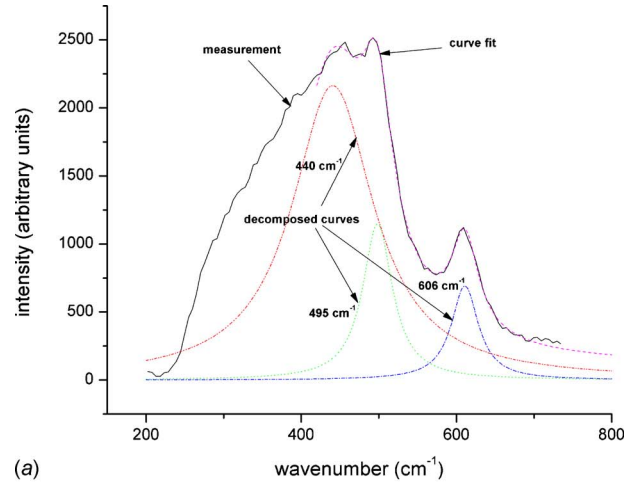
$$\Phi = \sum_{i=1}^n [Y_i - \hat{Y}_i]^2 \quad (7)$$

where  $\hat{Y}_i$  is the predicted value of the independent variable. In the case of nonlinear functions, although the contours of the  $\beta$ 's are distorted, they are almost elliptical in the vicinity of the minimum values of  $\Phi$ . The method works as follows. The initial population values are replaced by a new estimate  $\beta + \delta$  in each iteration step and equations are linearized in order to solve for  $\delta$

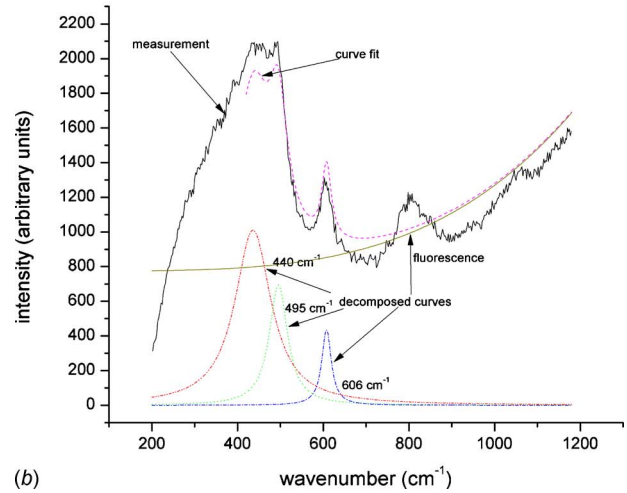
$$f(x, (\beta + \delta)) = f(x, \beta) + \frac{\partial f(x, \beta)}{\partial \beta} \times \delta \quad (8)$$

Once  $\delta$  is obtained, the new trial vector  $\beta^{(r+1)} = \beta^{(r)} + \delta^{(r)}$  will lead to the new sum of least-squares that, in the case of proper convergence, is smaller than 1 in previous iteration

$$\Phi^{(r+1)} < \Phi^{(r)} \quad (9)$$



(a)



(b)

**Fig. 5 Curve fit and decomposition of the typical Raman spectra in the fused silica treated with femtosecond laser pulses of 30  $\mu\text{J}$  energy: (a) without fluorescence at feed rate 1 mm/s and (b) taking fluorescence into account at feed rate 0.04 mm/s**

## 5 Results and Discussion

### 5.1 Modification of the Structure of the Random Network in Fused Silica

**5.1.1 Normalized Raman Spectra.** Before discussing the decomposition of the Raman spectra, spectra normalized to the maximum intensity under different processing conditions have been compared. Such normalized spectra at three different feed rates and the same pulse energy of 30  $\mu\text{J}$ , as well as reference spectra are superposed in Fig. 4. Chan et al. [11] stated that an increase in femtosecond laser pulse energy leads to relative increases in the intensity of the 495  $\text{cm}^{-1}$  and 606  $\text{cm}^{-1}$  peaks. Geissberger and Galeener [14] showed a similar response with increasing fictive temperature of the glass. It is assumed that this increase comes from the change of breathing modes between three- and four-membered rings, resulting in a change in bond angles between atoms and leads to the densification of the target material, as explained in detail in previous sections. From Fig. 4, it can be seen that a similar trend is present when a constant femtosecond laser pulse energy is applied but with different processing velocity. Also, it is noted that lines made using feed rates of 1 mm/s and 0.5 mm/s do not experience increases in fluorescence in opposition to the line created using 0.04 mm/s stage velocity, where a substantial increase in fluorescence is observed, which will be discussed in later sections.

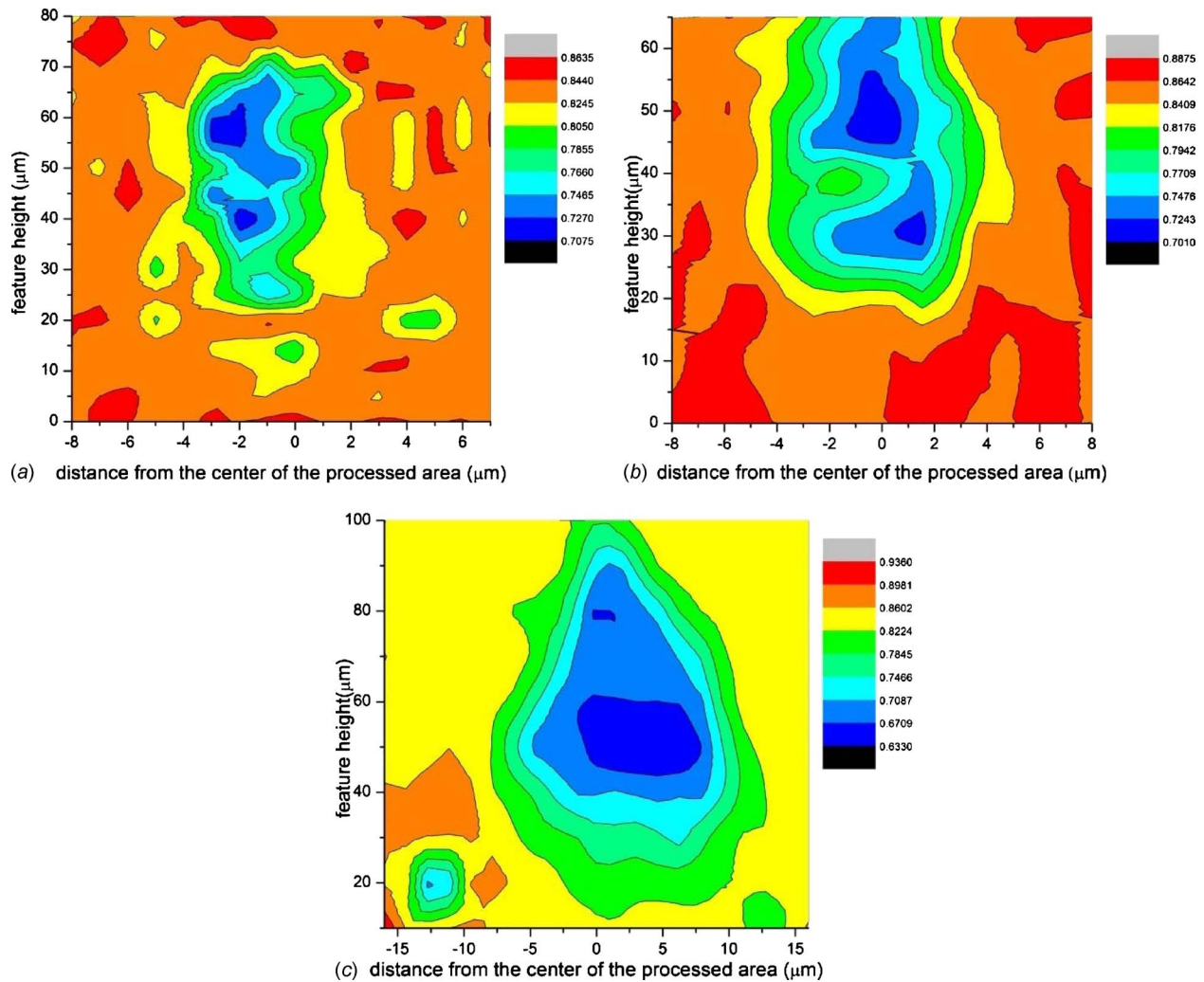


**Fig. 6** Volume fraction distribution of five- and six-membered rings based on the  $440 \text{ cm}^{-1}$  peak in Raman spectra of cross section of laser-irradiated region pulse energy  $30 \text{ } \mu\text{J}$  and feed rates: (a)  $1 \text{ mm/s}$ , (b)  $0.5 \text{ mm/s}$ , and (c)  $0.04 \text{ mm/s}$

**5.1.2 Decomposition of Raman Spectra.** The region of interest in Raman spectra obtained from a fused silica sample irradiated with a femtosecond laser lies between wave numbers  $300 \text{ cm}^{-1}$  and  $630 \text{ cm}^{-1}$ . Three distinctive peaks were observed in that region corresponding to the different ring structures. It is assumed that vibrational bands in the irradiated volume give the same Raman scattering. The line-profiles of the bands are Lorentzians, as discussed in detail in previous sections. Broadening of the main ( $440 \text{ cm}^{-1}$ ) peak is associated with the presence of higher order ring structures [12]. The content of higher membered ring structures in fused silica is small [25] and thus the broadening of the  $440 \text{ cm}^{-1}$  can be neglected. Therefore, this peak is fitted with a Lorentzian curve. It is assumed that within the volume of interest, four different structures coexist three-, four-, five-, and six-membered rings. Furthermore, the integrated intensity under Raman peaks corresponds to the percentage volume fraction of the different structures within the probed volume.

Decomposition of the spectrum was done through a curve fitting process. Two fitting functions were employed, one composed by superposing three Lorentz functions

$$y = y_0 + \frac{2A_1}{\pi} \frac{w_1}{4(x - x_{c1})^2 + w_1^2} + \frac{2A_2}{\pi} \frac{w_2}{4(x - x_{c2})^2 + w_2^2} + \frac{2A_3}{\pi} \frac{w_3}{4(x - x_{c3})^2 + w_3^2} \quad (10)$$

where  $x$  is an independent variable, in our case wave number,  $x_{ci}$  are peak positions,  $A_i$  are areas under the curve, and  $w_i$  are curve widths. An additional term has been added for analysis of the Raman spectra obtained from the fused silica sample processed using  $30 \text{ } \mu\text{J}$  pulse energy and  $0.04 \text{ mm/s}$  stage feed rate [26]. In this case, the target material modification is thermal in nature, which has the consequence of inducing fluorescence [27,28] that has to be taken into account. Fluorescence in essence represents the influence of the localized defects, which will be discussed in detail in following sections. Presence of fluorescence affects the reconfiguration of the ring structures, which is compensated for by adding another term [29,30] to Eq. (10),  $C \exp(-(x/t_1)^b)$ , which is Kohlraush–Williams–Watts (KWW) function, also known as a stretched exponential function. The KWW function is an empirical description of fluorescence decay, where  $x$  is an independent variable, as in Eq. (10),  $C$  is the proportionality coefficient,  $b$  is the stretching parameter and ranges between 0 and 1, and  $t_1$  is usually referred to as the characteristic relaxation time but, in this study, is treated as a free parameter.

Width, height, and area under the peaks were treated as free parameters. Peak positions, although known, were also treated as free parameters because, due to the spectroscopic precision, they were not located at their exact theoretical locations. Allowing them to be varied, which was not by more than a few wave numbers from their theoretical values, increased the quality of the fit

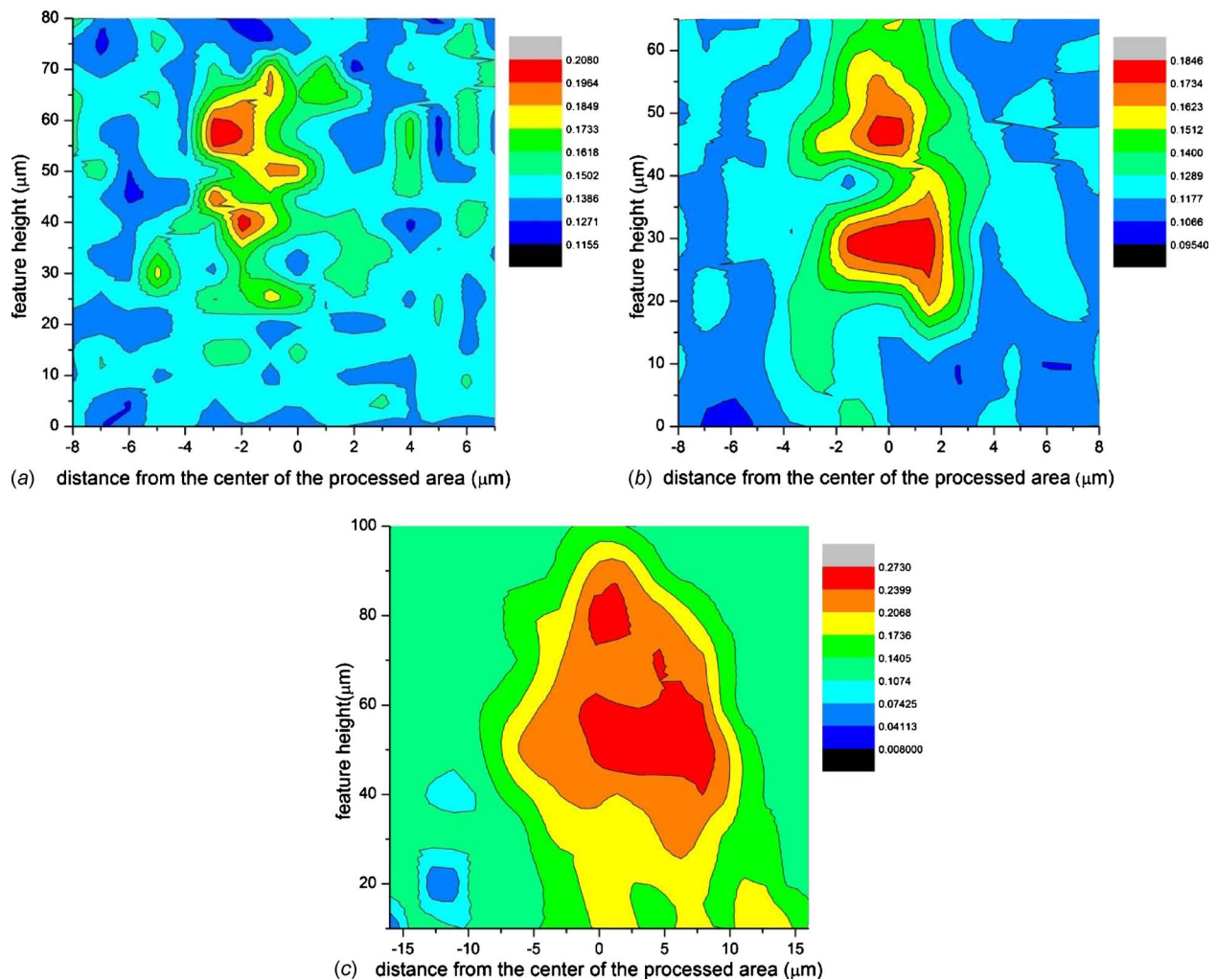


**Fig. 7** Volume fraction distribution of four-membered rings based on the  $495\text{ cm}^{-1}$  peak in Raman spectra of cross section of laser-irradiated region pulse energy  $30\ \mu\text{J}$  and feed rates: (a)  $1\text{ mm/s}$ , (b)  $0.5\text{ mm/s}$ , and (c)  $0.04\text{ mm/s}$

without compromising its accuracy. Initial guesses for the variables related to the  $495\text{ cm}^{-1}$  and  $606\text{ cm}^{-1}$  bands were taken from the analytical results found in Ref. [25]. Initial guesses for the variables associated with the  $440\text{ cm}^{-1}$  peak were found through fitting of this part of the Raman spectrum with a single Lorentzian because the main peak is three orders of magnitude larger than  $495\text{ cm}^{-1}$  and  $606\text{ cm}^{-1}$  peaks.

Decomposition of the Raman spectra in the center of the affected region for two different conditions, one with fluorescence and one without fluorescence, is depicted in Fig. 5. The sum of the integrated intensities under the main  $D_1$  and  $D_2$  peaks was assumed to correspond to 100% of the all  $n$ -fold rings within the probed volume. Furthermore, the ratio between the integrated intensity of a particular  $n$ -fold ring and the total integrated intensity represented the percentage of that ring structure in the probed volume. It should be noted that for the case with fluorescence, peaks corresponding to the  $\omega_3$  and  $\omega_4$  vibrational frequencies and located at wave numbers  $800\text{ cm}^{-1}$  and  $1100\text{ cm}^{-1}$ , respectively, were not taken into account in this study because they do not influence results in the region of interest. From Fig. 5(b), it can be seen that the fluorescence curve is not very steep in the region of interest, indicating that its contribution to the change of the ratio between integrated intensities of the  $n$ -fold rings is rather minor. However, for greater accuracy, fluorescence should be taken into account when fitting appropriate spectra.

**5.1.3 Cross-Sectional Contour Maps of Raman Spectra.** Figures 6–8 depict cross section contour maps of the change in the five- and six- and four- and threefold ring members, respectively. Three conditions are shown: laser pulse energy is held constant at  $30\ \mu\text{J}$  for all samples but feed rates vary and are  $1\text{ mm/s}$ ,  $0.5\text{ mm/s}$ , and  $0.04\text{ mm/s}$ , respectively. In addition, Fig. 9 extracts the percentage change of the given  $n$ -fold rings along the lateral direction ( $x$ -axis) passing the center of the irradiated region for comparison purposes. As seen from Figs. 6–8, the shape and size of the affected regions are qualitatively consistent with cross-sectional optical micrographs shown in part I of this study (noting that the  $x$ - and  $y$ -axis scales are quite different in each of Figs. 6–8). The percentage of  $n$ -fold rings in the unaffected area is compared with the predictions of the molecular dynamics model used by Rino et al. [16]. Their model predicts about 1% of the three-membered rings and 8% of the four-membered rings in the equilibrium condition. Our experimental findings give approximately 1.8% (Fig. 8) and 11.8% (Fig. 7) of three- and four-membered rings, respectively.

Figure 6 shows the content of five- and sixfold ring members in the cross section of the irradiated area. It can be seen that the content of higher membered rings decreases sharply from the untreated region toward the center of the focal volume, where laser intensity is highest. Also, it should be noted that two regions can be distinguished, an inner region, where the content of the five-

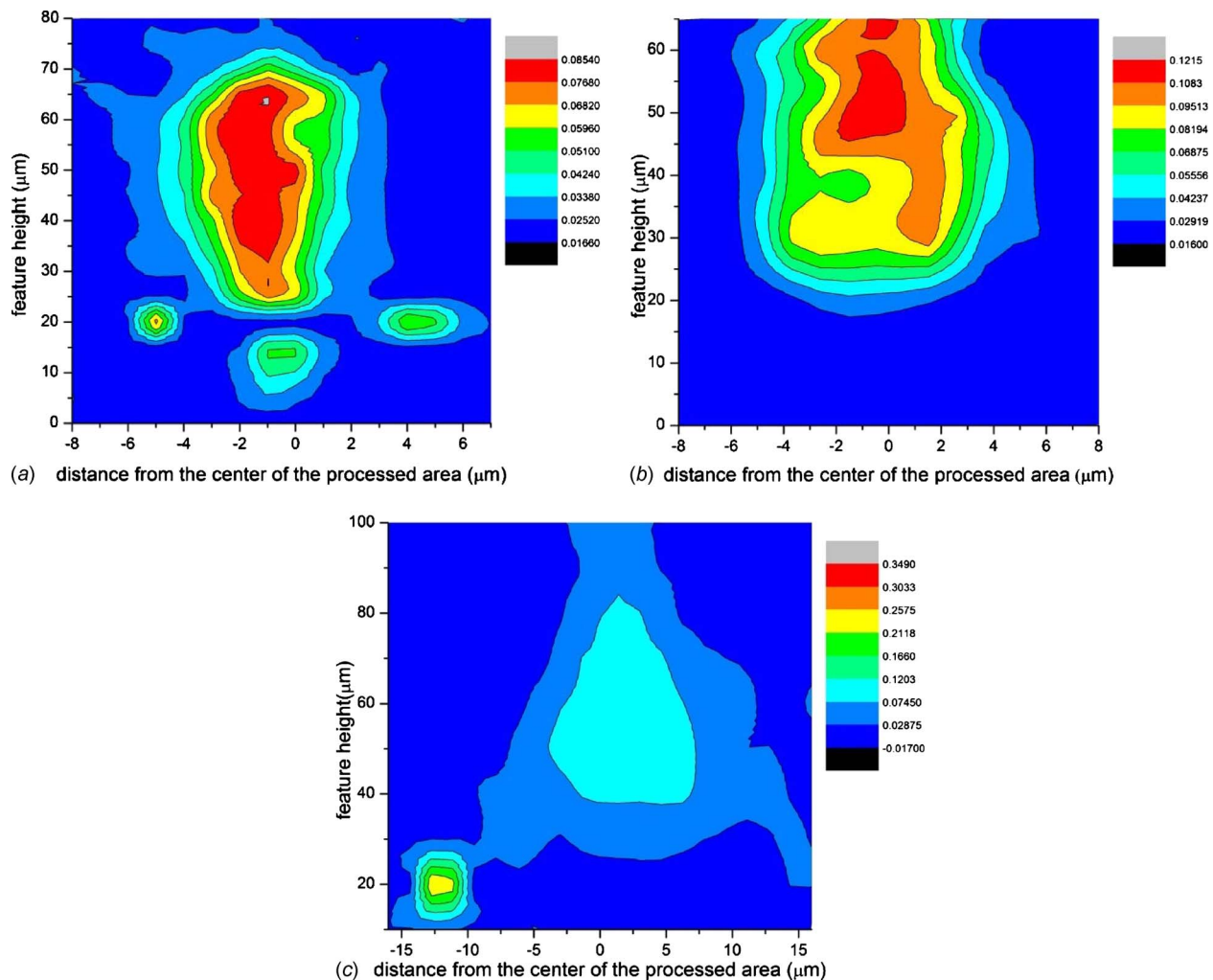


**Fig. 8** Volume fraction distribution of three-membered rings based on the  $606\text{ cm}^{-1}$  peak in Raman spectra of cross section of laser-irradiated region pulse energy  $30\text{ }\mu\text{J}$  and feed rates: (a)  $1\text{ mm/s}$ , (b)  $0.5\text{ mm/s}$ , and (c)  $0.04\text{ mm/s}$

and sixfold ring members is lowest and constant, and an outer region, where it gradually increases to the equilibrium value. The inner region might be associated with the focal volume, where change is abrupt due to rapid solidification, leaving the material frozen and the outer region would, in that case, be the surrounding affected region. The drop in percentage of five- and sixfold ring structures is the highest in the  $0.04\text{ mm/s}$  case to about 65% (Figs. 6 and 9(a)). This perhaps is due to the fact that this sample experiences the highest energy input, which causes the higher order rings to be converted to lower order ones.

Contour maps of the fourfold ring structures, associated with the  $495\text{ cm}^{-1}$  peak, are shown in Fig. 7. A similar trend to the one observed in Fig. 6 is seen here. Two different regions, inner and outer, can be differentiated; contour maps show that the modified area is narrower and shorter than in the case of three-, five-, and sixfold rings, suggesting that higher intensity is necessary to alter existing structures into four-membered rings. An analogous observation is made in amorphous fused silica treated by neutron irradiation, where it was shown that the intensity of the  $606\text{ cm}^{-1}$  band increases at a faster rate than the  $495\text{ cm}^{-1}$  band [14]. In the map corresponding to the  $1\text{ mm/s}$  feed rate, the feature appears to be scattered with a small and broken inner region. The percentage of fourfold ring structures goes up to 20%. The map corresponding to the  $0.5\text{ mm/s}$  feed rate is similar in length to the previous one but it is wider and the inner region is more established. The map corresponding to the  $0.04\text{ mm/s}$  feed rate is almost the same

in size and distribution as the one associated with the five- and sixfold rings, suggesting that the thermal mechanism of feature generation [26] causes different material response.

Similar to the previous two cases, contour maps for threefold rings, associated with the  $606\text{ cm}^{-1}$  peaks, are shown in Fig. 8. Here, one difference in the overall trend is observed. Unlike the contour maps related to the  $1\text{ mm/s}$  and  $0.5\text{ mm/s}$  feed rates that are similar in size and distribution to ones corresponding to the  $440\text{ cm}^{-1}$  peak, maps related to the case with  $0.04\text{ mm/s}$  velocity show an abrupt but not significant change in content of three-membered rings within the area of interest, a sharp distinction between the inner and outer regions, and an absence of gradient between the two.

Figure 9 extracts from Figs. 6–8 the volume fraction change of  $n$ -membered ring structures along the lateral direction ( $x$ -axis) within the cross section. The lines are chosen such that they pass through centers of the inner regions and it is representative of the structural alterations in the middle of the cross section. From the figures, it appears that for the features generated with  $1\text{ mm/s}$  and  $0.5\text{ mm/s}$  feed rates, transformation from five- and six- into three- and four-membered ring structures is quite similar. In part I of this study, it is stated that the mechanism responsible for feature generation at  $1\text{ mm/s}$  is explosive plasma expansion (EPE), which creates voxels in the center of the affected region with a desired surrounding region. However, from differential interference con-

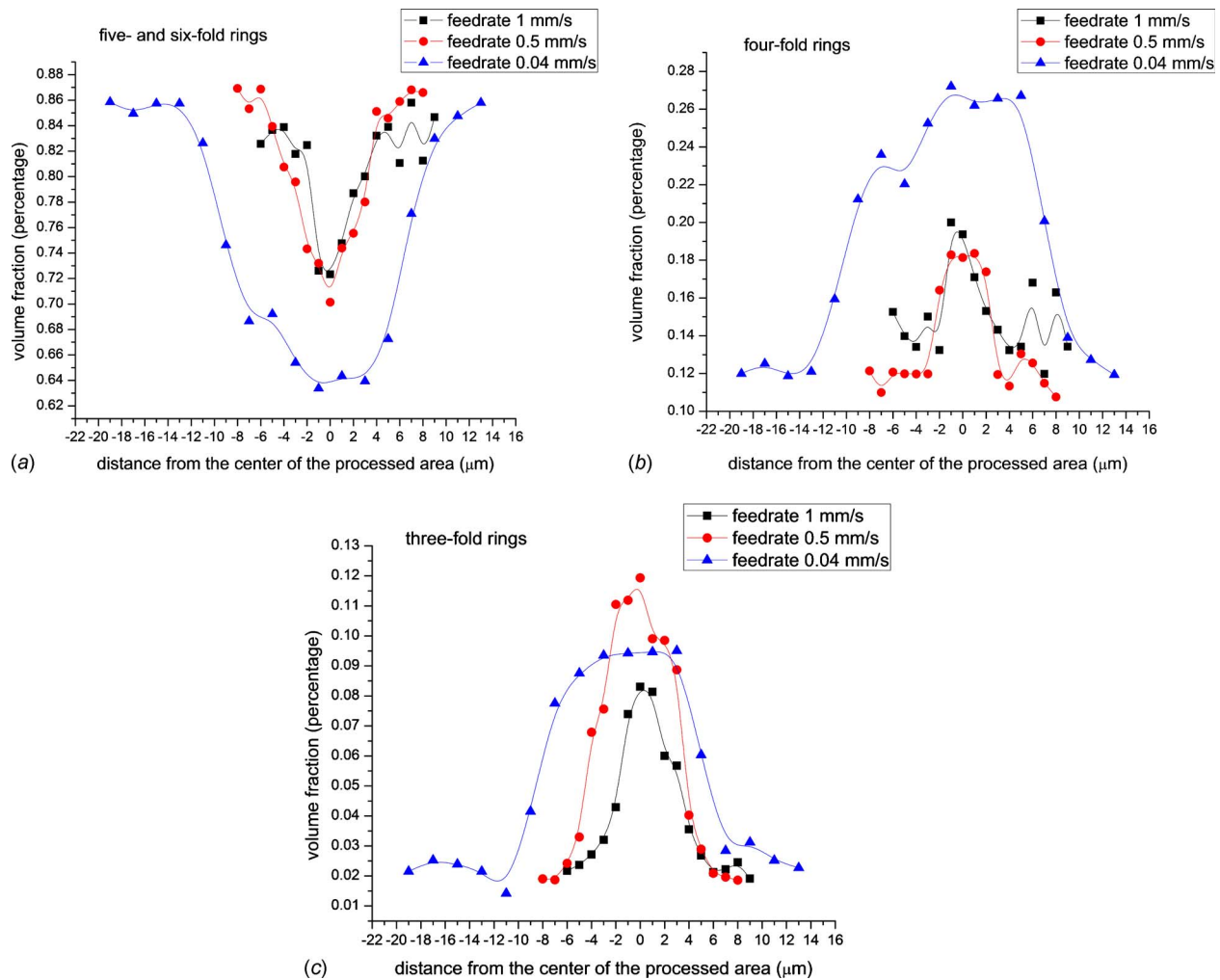


**Fig. 9** Volume fraction change of  $n$ -membered rings along the lateral direction within cross section: (a) five- and six-membered ring structures,  $440 \text{ cm}^{-1}$ , (b) four-membered ring structures,  $495 \text{ cm}^{-1}$ , and (c) three-membered ring structures,  $606 \text{ cm}^{-1}$

trast (DIC) optical micrographs [26], it was not clear if features generated with  $0.5 \text{ mm/s}$  stage velocity were also made under a similar mechanism. Two regions were distinguished: the upper one revealed a thermal origin, whereas in the lower one, cracklike formations appeared. From the Raman spectroscopy results presented here, it can be concluded that at the atomic level, structural alterations that take place are the same as for the EPE mechanism. However, more threefold ring structures are created using a  $0.5 \text{ mm/s}$  feed rate than  $1.0 \text{ mm/s}$ , which is consistent with previous observations in fused silica exposed to the neutron bombardment [14] in that with increases in deposited energy, the percentage of three-membered ring structures rises faster than four-membered ones. On the other hand, when a  $0.04 \text{ mm/s}$  feed rate is used, a thermal mechanism is primarily responsible for the modification of the target material. The affected region is much bigger and the percentage changes are larger. However, it appears that the increase of three-membered rings within the area of interest is similar to the previous two cases, which are counterintuitive, given the amount of energy deposited into the specimen. Also, the left shoulder of the main peak in the Raman spectra does not deviate much from the reference spectra (Fig. 4), as discussed previously, suggesting that most of the laser energy deposited into the target material is used for transformation of five- and sixfold rings into the four-membered ring structures (Figs. 9(a) and 9(b)) and the creation of defects, which will be discussed in Sec. 5.2.

**5.2 Fluorescence.** The nature of the defects present in amorphous glasses has been studied extensively, both theoretically and experimentally, and several models have been proposed [27,31]. It is stated that defects are induced by irradiation with various sources, such as gamma and X-rays, neutron bombardment, and studied by employment of electron spin resonance (ESR) and PL. More recently, the origin of fluorescence after laser treatment of fused silica with both nanosecond and femtosecond lasers has been characterized via PL and Raman spectroscopy. It has been reported that nanosecond laser treatment induces ODC and NBHOC in fused silica [10]. In Raman studies of fused silica irradiated by ultrafast lasers [10,28], presence of fluorescence is attributed to NBHOC, which represent point defects that consists of one half permanently broken Si–O bond, resulting in the oxygen atom being connected to only one  $\text{SiO}_4$  tetrahedron and thus not “bridge” two silicon atoms. Reichman et al. [28] reported that fluorescence increases from the periphery of the irradiated region toward its center, indicating an increase in the concentration of the defects. A similar trend is observed in this study when a  $0.04 \text{ mm/s}$  feed rate and  $30 \mu\text{J}$  pulse energy is used, suggesting that a significant amount of NBHOC defects is created only when the thermal modification mechanism takes place. As seen in Fig. 4, Raman spectra from the samples created with the same pulse energy but higher feed rates do not show the presence of fluores-

cence, indicating that when the explosive plasma expansion feature generation mechanism takes place, creation of microscale voxels occurs, as discussed in part I of this study, but it is not accompanied with atomic scale defects (refer to part I).

## 6 Conclusion

The portion of the Raman spectra that corresponds to the pure bending (symmetric stretch) motion of the oxygen atom has been investigated and obtained spectra were analyzed through decomposition into peaks corresponding to the various  $n$ -fold ring structures. A new quantitative method for analysis of the structural rearrangement of ring structures has been proposed. The method consists of spatially resolved identification of the volume fraction of ring structures within the probed volume through examination of Raman spectra. Reconfiguration of the random network and in particular, the ring structures of fused silica on irradiation via femtosecond laser pulses has been studied. Cross-sectional maps of three-, four-, five-, and six-membered rings were obtained. Two regions are formed: an inner region with a high and constant content of newly formed three- and four-membered rings and an outer one in which the amount of the rings decreases gradually with distance from the center. The inner region is associated with the focal volume and the outer one with the affected surrounding material. An opposite trend is observed in five- and six-membered ring maps. Three different processing conditions, thermal, in-between, and explosive plasma expansion feature generation mechanisms have been examined and our study has shown that upon irradiation with femtosecond lasers, the random network of fused silica reconfigures and the initially low presence of energetically unfavorable three- and four-membered rings increases at the expense of five- and six-membered rings. Furthermore, our study has shown that with decreasing feed rate at constant pulse energy, the percentage of three-membered rings increases rapidly, which is due to the change in mechanism responsible for the feature formation. Fluorescence in samples processed under the thermal mechanism has been observed and its presence linked with the formation of defects.

## Acknowledgment

The authors would like to thank Prof. John R. Lombardi of the City University of New York and Dr. Tommaso Baldacchini of Newport/Spectra-Physics for useful discussions. Assistance in preparing figures by Mr. Haohao Jiao is also gratefully acknowledged.

## References

- [1] Shirk, M. D., and Molian, P. A., 1998, "A Review of Ultrashort Pulsed Laser Ablation of Materials," *J. Laser Appl.*, **10**(1), pp. 18–28.
- [2] Stuart, B. C., Feit, M. D., Rubenchik, A. M., Shore, B. W., and Perry, M. D., 1995, "Laser-Induced Damage in Dielectrics With Nanosecond to Subpicosecond Pulses," *Phys. Rev. Lett.*, **74**(12), pp. 2248–2251.
- [3] Jiang, L., and Tsai, H. L., 2003, "Femtosecond Lasers Ablation: Challenges and Opportunities," NSF Workshop on Unsolved Problems and Research Needs in Thermal Aspects of Material Removal Processes, Stillwater, OK.
- [4] Glezer, E. N., Milosavljevic, M., Huang, L., Finlay, R. J., Her, T.-H., Callan, J. P., and Mazur, E., 1996, "Three-Dimensional Optical Storage Inside Transparent Materials," *Opt. Lett.*, **21**(24), pp. 2023–2025.
- [5] Glezer, E. N., and Mazur, E., 1997, "Ultrafast-Laser Driven Micro-Explosions in Transparent Materials," *Appl. Phys. Lett.*, **71**(7), pp. 882–884.
- [6] Bellouard, Y., Colomb, T., Depeursinge, C., Said, A. A., Dugan, M., and Bado, P., 2006, "Investigation of Femtosecond Laser Irradiation on Fused Silica," *Proc. SPIE*, **6108**, pp. 155–160.
- [7] Schaffer, C. B., Brodeur, A., Garcia, J. F., and Mazur, E., 2001, "Micromachining Bulk Glass by Use of Femtosecond Laser Pulses With Nanojoule Energy," *Opt. Lett.*, **26**(2), pp. 93–95.
- [8] Schaffer, C. B., Garcia, J. F., and Mazur, E., 2003, "Bulk Heating of Transparent Materials Using a High-Repetition-Rate Femtosecond Laser," *Appl. Phys. A: Mater. Sci. Process.*, **76**, pp. 351–354.
- [9] Schaffer, C. B., Jamison, A. O., and Mazur, E., 2004, "Morphology of Femtosecond Laser-Induced Structural Changes in Bulk Transparent Materials," *Appl. Phys. Lett.*, **84**(9), pp. 1441–1443.
- [10] Kucheyev, S. O., and Demos, S. G., 2003, "Optical Defects Produced in Fused Silica During Laser-Induced Breakdown," *Appl. Phys. Lett.*, **82**(19), pp. 3230–3232.
- [11] Chan, J. W., Huser, T., Risbund, S., and Krol, D. M., 2001, "Structural Changes in Fused Silica After Exposure to Focused Femtosecond Laser Pulses," *Opt. Lett.*, **26**(21), pp. 1726–1728.
- [12] Sharma, S. K., Mammone, J. F., and Nicol, M. F., 1981, "Raman Investigation of Ring Configurations in Vitreous Silica," *Nature (London)*, **292**, pp. 140–141.
- [13] Galeener, F. L., and Mikkelsen, J. C., Jr., 1981, "Vibrational Dynamics in  $^{18}\text{O}$ -Substituted Vitreous  $\text{SiO}_2$ ," *Phys. Rev. B*, **23**(10), pp. 5527–5530.
- [14] Geissberger, A. E., and Galeener, F. L., 1983, "Raman Studies of Vitreous  $\text{SiO}_2$  Versus Fictive Temperature," *Phys. Rev. B*, **28**(6), pp. 3266–3271.
- [15] King, S., 1967, "Ring Configurations in a Random Network Model of Vitreous Silica," *Nature (London)*, **213**, pp. 1112–1113.
- [16] Rino, J. P., Ebbsjo, I., Kalia, R. K., Nakano, A., and Vashishta, P., 1993, "Structure of Rings in Vitreous  $\text{SiO}_2$ ," *Phys. Rev. B*, **47**(6), pp. 3053–3062.
- [17] Bell, R. J., and Dean, P., 1966, "Properties of Vitreous Silica: Analysis of Random Network Models," *Nature (London)*, **212**, pp. 1354–1356.
- [18] Vashishta, P., Kalia, R. K., Rino, J. P., and Ebbsjö, I., 1990, "Interaction Potential for  $\text{SiO}_2$ : A Molecular-Dynamics Study of Structural Correlations," *Phys. Rev. B*, **41**(17), pp. 12197–12209.
- [19] Galeener, F. L., Barrio, R. A., Martinez, E., and Elliot, R. J., 1984, "Vibrational Decoupling of Rings in Amorphous Solids," *Phys. Rev. Lett.*, **53**(25), pp. 2429–2432.
- [20] Sen, P. N., and Thorpe, M. F., 1977, "Phonons in  $\text{AX}_2$  Glasses: From Molecular to Band-Like Modes," *Phys. Rev. B*, **15**(8), pp. 4030–4038.
- [21] Galeener, F. L., 1982, "Planar Rings in Glasses," *Solid State Commun.*, **44**(7), pp. 1037–1040.
- [22] Galeener, F. L., 1979, "Band Limits and the Vibrational Spectra of Tetrahedral Glasses," *Phys. Rev. B*, **19**(8), pp. 4292–4297.
- [23] Galeener, F. L., and Lucovsky, G., 1976, "Longitudinal Optical Vibrations in Glasses-  $\text{GeO}_2$  and  $\text{SiO}_2$ ," *Phys. Rev. Lett.*, **37**(22), pp. 1474–1478.
- [24] Marshall, A. G., and Verdun, F. R., 1990, *Fourier Transforms in NMR, Optical and Mass Spectrometry*, Elsevier, Amsterdam.
- [25] Pasquarello, A., and Car, R., 1998, "Identification of Raman Defect Lines as Signatures of Ring Structures in Vitreous Silica," *Phys. Rev. Lett.*, **80**(23), pp. 5145–5147.
- [26] Vukelić, S., Kongsuwan, P., and Yao, Y. L., 2010, "Ultrafast Laser Induced Structural Modification of Fused Silica—Part I: Feature Formation Mechanisms," *ASME J. Manuf. Sci. Eng.*, **132**(6), p. 061012.
- [27] Skuja, L. N., and Silin, A. R., 1982, "A Model for the Non-Bridging Oxygen Center in Fused Silica," *Phys. Status Solidi A*, **70**, pp. 43–49.
- [28] Reichman, W., Chan, J. W., and Krol, D. M., 2003, "Confocal Fluorescence and Raman Microscopy of Femtosecond Laser-Modified Fused Silica," *J. Phys.: Condens. Matter*, **15**, pp. S2447–S2456.
- [29] Meier, R. J., 2005, "On Art and Science in Curve-Fitting Vibrational Spectra," *Vib. Spectrosc.*, **39**(2), pp. 266–269.
- [30] Hughes, M., Hewak, D. W., and Curry, R. J., 2007, "Concentration Dependence of the Fluorescence Decay Profile in Transition Metal Doped Chalcogenide Glass," *Proc. SPIE*, **6469**, p. 64690D.
- [31] Griscom, D. L., 1991, "Optical Properties and Structure of Defects in Silica Glass," *J. Ceram. Soc. Jpn.*, **99**(10), pp. 923–942.